Tunable Coprecipitation of $MnCO_3$ Templates for Synthesis of Li-ion Battery Materials

---

A Thesis

Presented to

the faculty of the School of Engineering and Applied Science

University of Virginia

---

in partial fulfillment

of the requirements for the degree

Master of Science

by

James Pierce Robinson

December

2015

APPROVAL SHEET

The thesis

is submitted in partial fulfillment of the requirements

for the degree of

Master of Science

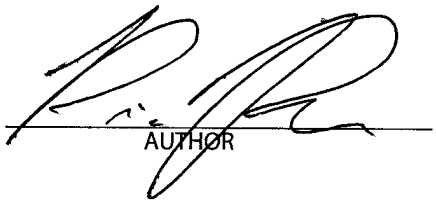

AUTHOR

The thesis has been read and approved by the examining committee:

Gary Koenig

Advisor

David Green

Joshua Choi

Accepted for the School of Engineering and Applied Science:

Craig H. Benson, Dean, School of Engineering and Applied Science

December

2015

Acknowledgements

First I would like to thank my advisor Gary Koenig for his mentorship and constructive attitude. I'd also like to thank my fellow Koenig lab group members Ethan Paharik, Colin Qi, Charles Michaelis, and Spring Dong for their friendship and assistance in the lab. I would also like to thank professors David Green and Joshua Choi for serving on my M.S. Committee.

Abstract

Many battery materials are synthesized via calcination of precursor particle powders with a lithium source. The precursor particles frequently are made via coprecipitation reactions and a number of combinations of coprecipitation agents have been demonstrated previously. Detailed control over the morphology of precursor particles and the resulting final electrode materials would be highly desirable, but currently detailed understanding of the impact of synthesis conditions on precursor morphology are lacking. Herein, tunable monodisperse $MnCO_3$ particles for Li-ion battery precursors of varying size and shape were synthesized through batch coprecipitation. The effect of solution chemistry on final particle morphology was confirmed via scanning electron microscopy and considered in the context of solution equilibrium calculations and nucleation and growth of precipitate crystals. The tunability of $MnCO_3$ particle morphology with reagent concentration was demonstrated with transitions from rhombohedra to cubes to spheres to smaller spheres with regards to overall secondary particle structures. Other experimental factors were also examined to further understand the processes resulting in the transitions in $MnCO_3$ morphology. Precursor particles were calcined to form $LiMn_2O_4$ to verify the ability to maintain the tunable morphology in the final battery materials and to confirm suitability for battery cathodes.

Table of Contents

List of Figures

List of Tables

1. Introduction

Lithium-ion batteries have become the dominant technology for consumer electronics applications and are increasingly being developed for larger-scale applications such as electric vehicle batteries and stationary energy storage.[1] While historically battery progress has largely been tracked by adoption of chemistries and materials structures with higher energy densities,[2,3,4] another important factor in battery performance is the morphology of the electrochemically active particles within the battery electrode as well as their organization and distribution within the composite structure. For example, the battery materials literature is full of the synthesis and characterization of materials with a wide variety of particle shapes and sizes, including rods,[5] cubes,[6] spheres,[7] urchins,[8] plates,[9] and many others.[10,11,12,13] In some cases, the morphology serves to provide preferential diffusion paths for lithium or conduction paths for electrons that improve rate capability or energy density of the battery material.[9] In other reports, the morphology is taken advantage of to organize the overall electrode structure to accommodate improvements in lithium-ion diffusion in and out of the electrode as a whole.[14] One of the key factors in being able to take advantage of active particle morphology-dependent improvements in battery electrode performance is that the electrode particle morphology must be well-controlled. Thus, underlying mechanisms that result in the final particle morphology with regards to size, shape, porosity, surface roughness, and polydispersity are important to engineering particles for battery electrodes. In addition, tunability of one or more of these morphology metrics would also be desirable. The study described herein focuses on efforts to control particle morphology in a battery electrode precursor particle system.

The chemistry employed to synthesize precursor particles in this study was coprecipitation of Mn^{2+} with carbonate salts to form $MnCO_3$. Coprecipitation was chosen as a

method because it is highly tunable and easily scalable for particle synthesis,[7,15,16] and $MnCO_3$ was chosen as a target precursor chemistry because it can be calcined with a lithium source to form the final battery material $LiMn_2O_4$.[17] Given the relatively lower complexity of only having one transition metal involved in the coprecipitation synthesis and the availability of data on $LiMn_2O_4$ in the battery literature,[18,19] $MnCO_3$ serves as a model system for precursor morphology tunability. A number of reports have previously been published in the literature on synthesis of transition metal carbonates, including $MnCO_3$, and a variety of particle morphologies that may be achieved.[11,20,21,22,23] Notably, the most commonly reported morphology for transition metal carbonates used for battery material templates is approximately spherical and has relatively high polydispersity.[11,24,25] The extent of the tunability of the morphologies and polydispersity of transition metal carbonate template particles, however, is currently unknown. The ability to be predictive in the resultant morphology of these particles would in principle enable detailed studies of the influence of particle morphologies on lithium-ion battery performance.

In general, the morphology of particles generated from coprecipitation reactions can be influenced by a variety of factors, including reagent concentrations, nucleation and growth rates, ripening, collisions with reactor walls and other particles, temperature, and chemical modifiers including chelating agents.[15,26,16] Due to the high level of complexity for consideration of all of these factors, we have focused our initial study on the influence of solution chemistry on particle morphology. In this paper, we will demonstrate a variety of particle morphologies that are accessible via relatively modest changes in coprecipitation solution chemistry. This variety is likely not driven by ripening processes that have been demonstrated to influence morphologies for other coprecipitation processes for battery particles previously reported in the literature for

hydroxide synthesis[26]. The conversion of our precursor particles to lithiated battery electrode active materials was also performed to demonstrate that the tunable morphologies can be retained in the resulting final electrode materials. While our solution chemistry approach is an initial report of understanding the morphology tunability of this battery precursor system, we speculate a wide design space of size, shape, and surface roughness control will be accessible via detailed study of this synthesis platform.

2. Background

2.1 Battery Particle Morphology Overview

Conventional Li-ion electrodes are composite materials typically including a high percentage of densely packed active material particles mixed with a small quantity of conductive additive and binder to impart electrical conductivity and mechanical strength respectively. This composite is usually soaked in a concentrated Li^+ liquid electrolyte providing a method to transport Li^+ between the crystal grains of active material particles. Ideal performance depends on balancing various transport resistances in the cell, particularly Li^+ and e^- transport in the active material particle which can often be mitigated through reducing particle size. On the other hand, large particles tend to pack more densely into the composite electrode ultimately resulting in a higher energy density in the device. Another important consideration affecting the lifetime of batteries is the volume-change induced stress in intercalation materials, a factor which is also mitigated by electrode and particle design.[27]

Without resorting to developing new materials and chemistries, battery energy densities can most easily be improved by increasing the packing fraction of active material in the electrode, or by creating a larger electrode relative to other battery components. Lowering the polarization in the cell by reducing internal transport resistances for electrons and lithium ions can also result in gains in energy density. Lithium mass transport limitations result in partial charges and discharge cycles at high rates, reducing the battery's effective energy density. Increasing the loading of active material particles must be done with a strategy to offset the added kinetic limitations due to having smaller channels for lithium ions. This push and pull between different geometric considerations in Li-ion electrode design is the basic reason for the desire to control particle morphology in order to optimize performance.

2.2 $MnCO_3$ Synthesis in the Literature.

Most examples of $MnCO_3$ coprecipitation in the literature produced polydisperse particles not suitable for detailed studies on particle morphology[11,24,25]; however, we found several examples of $MnCO_3$ templates which suggested that this material can be used to create tunable monodisperse precursors. A common approach in the coprecipitation literature is modulating the concentration of various ions in solution. One of the most successful $MnCO_3$ synthesis studies in this vein was done by Hamada et al.[21] By altering the $[CO_3^{2-}]/[Mn^{2+}]$ and $[SO_4^{2-}]/[Mn^{2+}]$ ratios the authors were able to produce monodisperse ~5 μm spheres and ~28 μm rhombohedra. Although not demonstrating tunability in particle size, this article demonstrated the potential monodispersity of $MnCO_3$ particles synthesized through a simple mixing process, and served as an inspiration for this work. SEM images of those $MnCO_3$ templates are shown in Figure 1.

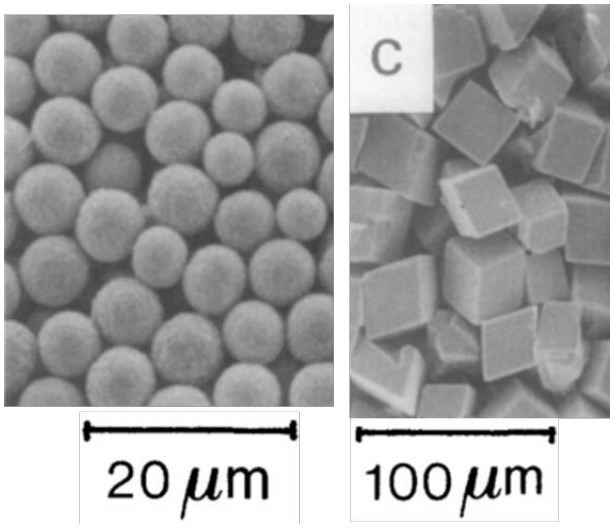

Figure 1. Monodisperse $MnCO_3$ templates produced by Hamada et al.[21]

Zhu et al. showed very tight $MnCO_3$ particle size control in the 3-9 μm range using a seeded growth system that apparently decoupled the nucleation and growth of $MnCO_3$.[22] Their

method was difficult to reproduce however and it was unclear how polydisperse the smaller average size particles were given the qualitative descriptions of size distributions in the article. This article also served as a benchmark to demonstrate the level of size control and monodispersity attainable in the synthesis of $MnCO_3$ microparticles. Some representative images are shown in Figure 2.

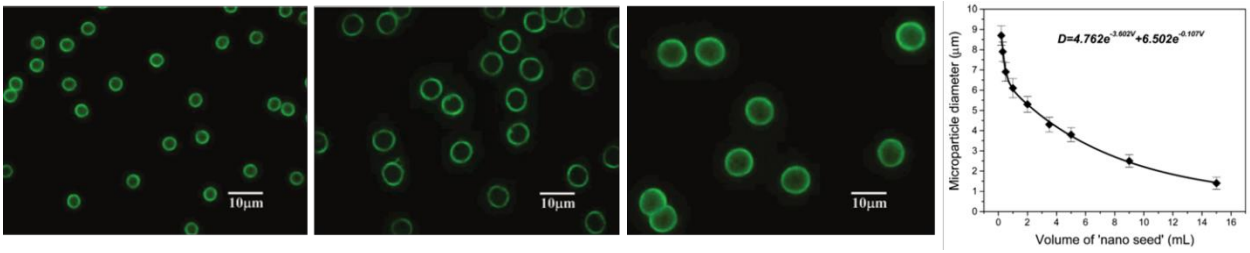

Figure 2. $MnCO_3$ particles of different diameters obtained by addition of different volumes of diute "nano seed" solution. The graph on the right shows the relationship between the number of seeds added and the resulting particle size. Figure taken from Zhu et al.

2.3 Solution Equilibria in the Metal Hydroxide Coprecipitation System

A possibility that we explored for making monodisperse $MnCO_3$ particles was a dissolution/recrystallization ripening process facilitated by ammonia as a chelating agent. This approach has been used by van Bommel and Dahn[26], who have demonstrated an equilibrium-based ripening mechanism for metal hydroxide particles precipitated in the presence of ammonia. Selected results from that article are shown in Figure 3.

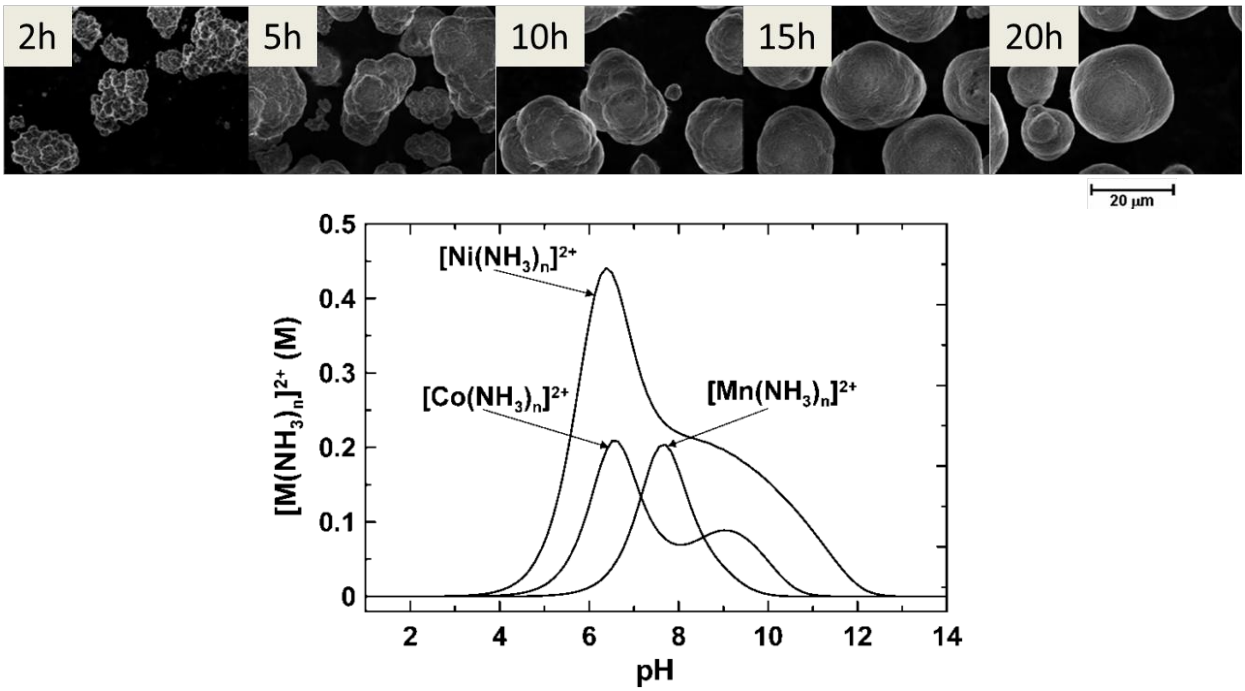

Figure 3. (Top) Time evolution of coprecipitated $Ni(OH)_2$ in the presence of ammonia. Particles gradually ripened leading to higher packing densities. (Bottom) Equilibrium calculation result showing the concentration of all metal-ammonia complexes in the $M(OH)_2$ system. Figure taken from van Bommel and Dahn.[26]

As can be seen in Figure 3, at a pH of around 7.5-8.0 the authors predicted a 0.2 M maximum in the level of complexed manganese, about $1/5^{th}$ of the total moles of Mn in their system. The chelation of Mn was primarily limited by the formation of NH_4^+ at low pH, and the formation of $Mn(OH)_2$ at high pH, leaving a "sweet spot" where the greatest portion of metal ions are complexed in solution. This allows for a ripening process where surface energy is minimized through transfer of mass from small particles to large particles.

The pH where chelation is at its peak in the hydroxide system, 7.5-8.0, is the pH range found in our $MnCO_3$ synthesis conditions. Knowing the importance of ammonia based on widespread usage in carbonate coprecipitation and our reported results, it seemed likely that

ammonia was playing a similar role in the CO_3^{-2} system, leading to the investigation of equilibrium concentrations described in Section 4.3.

2.4 Statement of Objectives

To summarize the preceding text, the objectives of this thesis are the following:

1. Obtain detailed understanding of the relationship between solution chemistry and $MnCO_3$ particle morphology.
2. Create a library of monodisperse $MnCO_3$ particle morphologies for the future use in studies on electrode architectures.
3. Investigate role of ripening mechanisms on $MnCO_3$ particle morphology, including the role of ammonia as a chelating agent.
4. Demonstrate the conversion of $MnCO_3$ precursors to $LiMn_2O_4$ active material with complete maintenance of secondary structure and good electrochemical properties.

3.0 Materials and Methods

3.1 Preparation of $MnCO_3$ and $LiMn_2O_4$ Particles

$MnCO_3$ particles were prepared as follows: 1200 mL of 1.5-240 mM NH_4HCO_3 (Fischer) in deionized (DI) water was poured all at once into 1200 mL of 1.5-12 mM $MnSO_4 \cdot H_2O$ (Fischer) in DI water solution in a 4 L beaker. Solutions were preheated to 50 °C prior to mixing and the temperature was maintained at 50 °C for the duration of the synthesis. The solution was stirred gently with an impeller at 500 rpm to prevent particle settling in solution and $MnCO_3$ particles were precipitated for 0.5 h. All syntheses were done at a pH of ~7.5. Vacuum filtration was used to collect the particles, and the particle cake was rinsed with 2 L DI water before being vacuum dried at 80 °C overnight. $MnCO_3$ particles were converted to $LiMn_2O_4$ particles through calcination after mixing stoichiometric quantities of LiOH in a Carbolite CWF 1300 box furnace in an air atmosphere at 800 °C for 5 h.

3.2 Material Characterization

Powder X-ray diffraction was performed with a PANalytical X'Pert Pro MPD using CuKα radiation. Scanning electron microscopy (SEM) with an FEI Quanta 650 SEM was used to image all samples. Particle size distributions were obtained by analysis of SEM images with the program ImageJ[28].

3.3 Electrochemical Characterization

Electrochemical analysis was done using CR2032 coin cells with lithium metal anodes and as-synthesized $LiMn_2O_4$ cathodes. The $LiMn_2O_4$-containing cathode was prepared by coating a slurry comprised of $LiMn_2O_4$ active material, carbon black

conductive additive, and polyvinylidene diflouride binder in a weight ratio of 80:10:10 onto an aluminum current collector. The electrode slurry was dried in an 80 °C oven overnight and dried in an 80 °C vacuum oven for 3 h prior to punching out 14 mm electrode disks. The electrolyte used was 1.2 M $LiPF_6$ dissolved in a solution containing 3:7 ethylene carbonate:ethyl methyl carbonate. Cells were cycled between a voltage window of 3.4 to 4.2 V vs Li/Li^+ using a MACCOR battery tester.

4. Results and Discussion

4.1 Review of obtained $MnCO_3$ Template Morphologies

In this study we specifically focused on the influence of solution chemistry on $MnCO_3$ particle morphology. We designed our experiments to systematically vary both the total Mn^{2+} initially in solution (via total amount of $MnSO_4$ salt originally dissolved in DI water) as well as the ratio of the dissolved transition metal to the coprecipitation agent. In our case, coprecipitation was facilitated by the CO_3^{2-} from dissolved NH_4HCO_3.

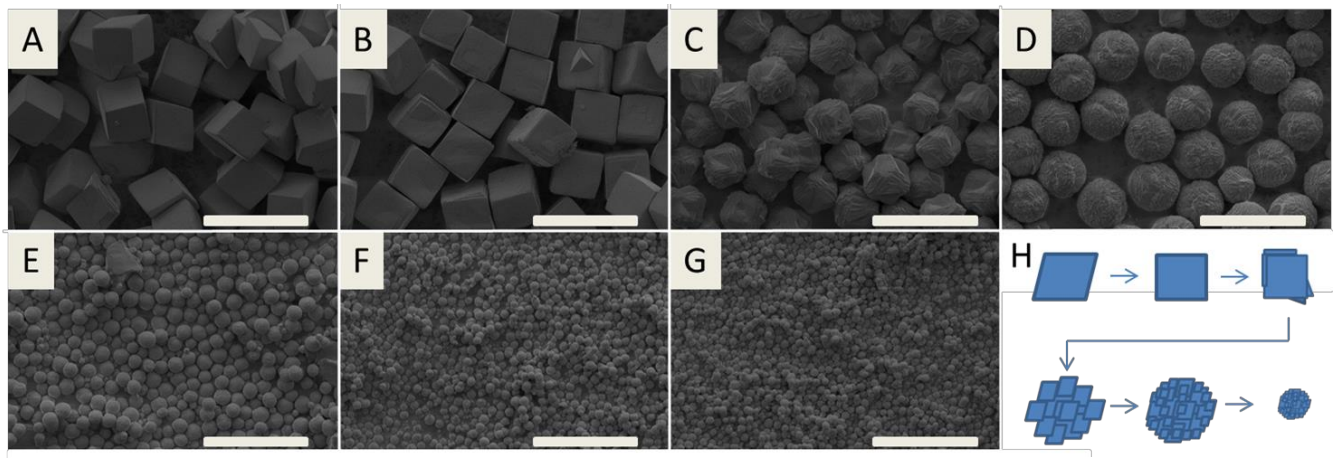

Figure 4. SEM images of $MnCO_3$ particles prepared with a 40:1 ratio of NH_4HCO_3 to $MnSO_4$ and ascending concentration of $MnSO_4$: (A) 1.5 mM $MnSO_4$, (B) 3 mM $MnSO_4$, (C) 4.5 mM $MnSO_4$, (D) 6 mM $MnSO_4$, (E) 7.5 mM $MnSO_4$, (F) 9 mM $MnSO_4$, (G) 10.5 mM $MnSO_4$. The particles from the 12 mM synthesis were not recoverable. Scale bars correspond to 20 μm. (H) Illustration of general shape and size transition of $MnCO_3$ at progressively higher concentration.

A representative example of the dramatic changes in $MnCO_3$ particle morphology facilitated by changes in total initial Mn^{2+} concentration (with constant NH_4HCO_3:$MnSO_4$ ratio of 40:1) can be found in the SEMs in Figure 4. At the lowest initial Mn^{2+} concentration (1.5 mM), particles were relatively large at just under 10 μm in average length of a particle side (Figure 4A). The particle surfaces appeared smooth and the overall shape was rhombohedral, with the wide angle measured to be ~103° from SEM

images. It should be noted that this was similar to the rhombohedral angles reported for single $MnCO_3$ crystals[29]. We also note that these particles have a large degree of clustering relative to others from the synthesis series shown in Figure 4, with particles often fused together. A slight increase in concentration from 1.5 to 3 mM initial Mn^{2+} resulted in a transition from a rhombohedral morphology to a cubical morphology (Figure 4B). The cubical particles were approximately the same size and the surfaces were smooth, however all angles on the particles were now ~90° and it was rare to find the cubical particles attached or clustered together. An increase in Mn^{2+} concentration to 4.5 mM resulted in particles that are in a transition region between cubical and spherical particles (Figure 4C). The average particle size (an approximate diameter assuming they were spherical) is not significantly different from the rhombohedra or cubes, however, there were many edges and corners on the surfaces of the particles and there was a flaky, layered appearance to the surface resulting in a large degree of surface roughness. There were no longer 8 sharp, obvious corners on the particle surface. At 6 mM Mn^{2+}, the resulting particles have transitioned to an approximately spherical morphology (Figure 4D). The diameters of the spherical particles were on approximately the same length scale as the particle length/diameters of the previously collected particles at lower Mn^{2+} concentrations. It was clear the overall spherical secondary particle morphology consisted of aggregates of smaller faceted particles that can be seen at the surfaces of the particles. A further increase in Mn^{2+} initial concentration to 7.5 mM resulted in spherical particles as well (Figure 4E). These particles were also clearly made up of smaller primary particle aggregates that have agglomerated into a secondary structure that was approximately spherical. Relative to the spherical particles at the slightly lower Mn^{2+} concentration

(Figure 4D), the average particle size has dropped significantly with the diameters decreasing by almost a factor of 4 (Figure 4E). Subsequent increases in initial Mn^{2+} concentration to 9 mM (Figure 4F) and 10.5 mM (Figure 4G) resulted in particle morphologies that were approximately spherical and similar to those found at 7.5 mM (Figure 4E), although as the Mn^{2+} concentration was increased the average diameter of the particles decreased slightly. We note that a final synthesis was done at 12 mM initial Mn^{2+} concentration; however, the particles were not recoverable for SEM characterization. A cartoon illustrating the transition from rhombohedral to cubical to transitionary cubical/spherical to spherical to decreasing diameter spherical is shown in Figure 4H to highlight the morphology changes from Figures 4A-G.

To gain further insights into the influence of reagent concentrations and solution chemistry on final $MnCO_3$ precipitate particle morpohology, a series of experiments were conducted where the same sequence of increasing Mn^{2+} concentrations was used as described earlier (1.5 to 12 mM in 1.5 mM increments, as used in Figure 4), however, the NH_4HCO_3:$MnSO_4$ ratio was varied as well with ratios of 10:1, 5:1, and 1:1 in addition to the 40:1 sequence described above. The detailed SEMs of the resulting particle morphologies can be found in the Appendix in Figure A1 (10:1 reagent ratio), Figure A2 (5:1 reagent ratio), and Figure A3 (1:1 reagent ratio). The morphologies observed are summarized in the illustration in Figure 5. At all NH_4HCO_3:$MnSO_4$ ratios the general trend for change in morphology was the same, where for increasing Mn^{2+} concentrations the particles transitioned from rhombohedral and/or cubical morphologies to a cubical/spherical transitional morphology to large spherical particles to decreasing sizes

of spherical particles. Also, as the NH_4HCO_3:$MnSO_4$ ratio decreased, the location of the cubical-to-spherical transition moved to higher initial Mn^{2+} reagent concentrations. At the lower NH_4HCO_3:$MnSO_4$ ratios, recovery of samples with the lowest concentrations of initial Mn^{2+} became less likely.

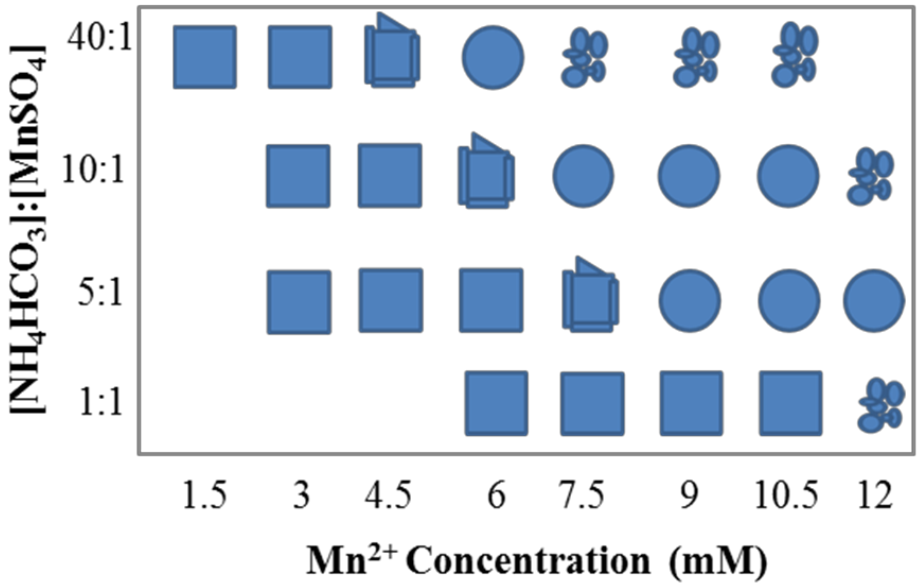

Figure 5. Ilustrations of morphology of $MnCO_3$ particles at prescribed synthesis conditions. Squares represent primarily rhombohedral or cubical particles, jagged squares represent cubical/spherical transitional particles, circles represent primarily spherical particles, and small circles represent small spherical particles. Blank locations denote conditions where particles were not recoverable.

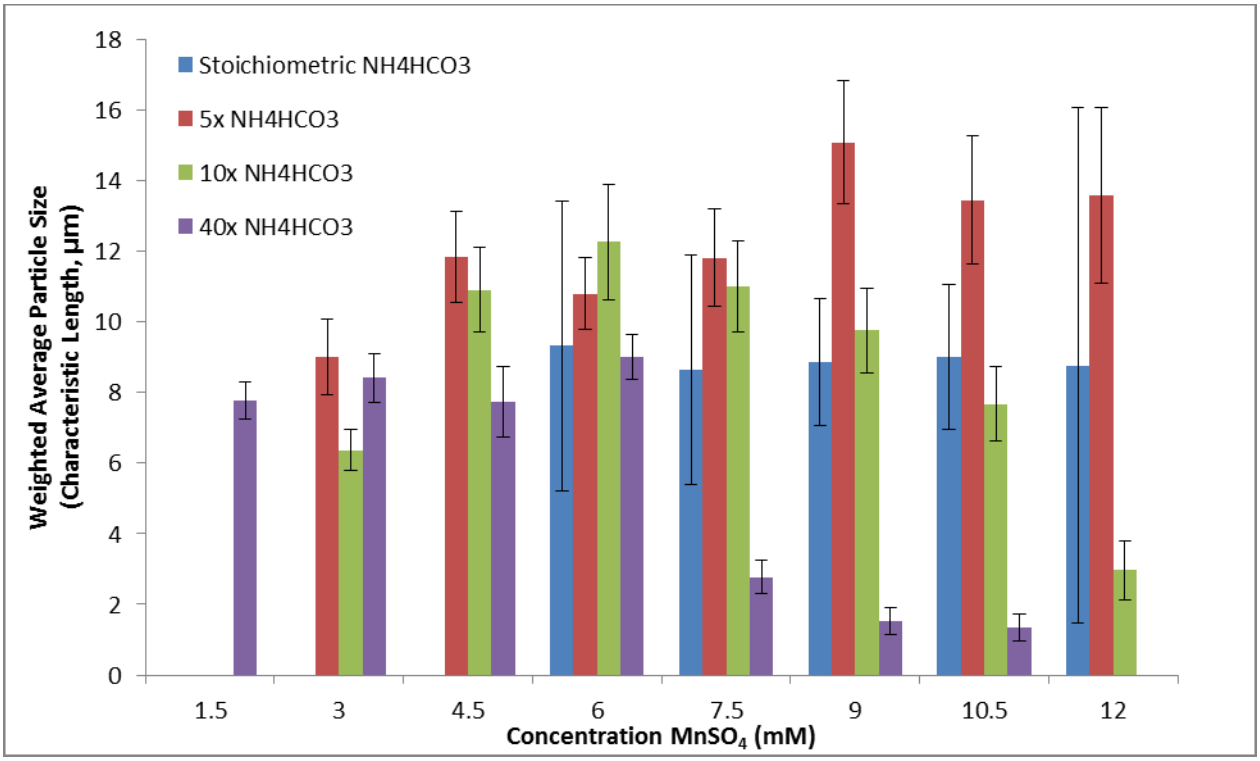

Figure 6. Volume weighted average particle size (characteristic length defined in text) at prescribed synthesis conditions. Error bars show one standard deviation.

Figure 6 displays the average particle size at the variety of synthesis conditions explored. Size was defined as the characteristic length of the particles (edge length for cubical or rhombohedral particles and diameter for transitional particles and spherical particles). The results displayed in Figure 5 demonstrate the diversity of particle morphologies and sizes that were accessible from the solution chemistry conditions investigated. The size range for smooth cubical/rhombohedral particles was 6-12 µm. Transitional cubical/spherical rough particles ranged in size from 8-12 µm. Spheres were synthesized in sizes ranging from 1-15 µm. We note that the polydispersity of these particles was very low compared to coprecipitation battery precursor synthesis typically

reported in the literature,[11,24,25] with many of our synthesized particle population polydispersities <10%.

4.2 Analysis of $MnCO_3$ Particle Formation

The morphology transitions observed in our solution synthesis were consistent with tuning the nucleation and growth of the $MnCO_3$ particles within the range of concentrations explored. At the lowest Mn^{2+} concentrations, the synthesis had the longest inoculation times (inoculation time being the time elapsed between mixing and visible precipitation in the beaker) indicating a slow growth of the precipitates. In this slow growth limit particles also had sharp angles that deviated from the 90° degree cubical particles and began to approach the wide rhombohedral angle of rhodochrosite ($MnCO_3$), which has been reported as 103°.[29] The slow growth of the particles and angles of the particles observed being around 103° was consistent with the particles approaching the single crystal limit of $MnCO_3$ (Figure 4A), thus it was likely that these particles were single rhodochrosite crystals. At increasing Mn^{2+} concentrations, inoculation times were always observed to decrease. The decreased inoculation time would result in more small nuclei precipitates being formed. At the highest Mn^{2+} concentrations, this would be consistent with the decrease in spherical particle size observed for increasing Mn^{2+} concentrations (Figures 4D-G). With more nuclei being produced because of the high initial precipitate reagent concentration, there was less reagent available for growth on a per particle basis and thus the final resulting particles were smaller for higher reagent concentrations. Correlations between higher nuclei density and smaller final particle populations have previously been reported for $MnCO_3$ synthesis.[22] It is important to note,

however, that our spherical particles were agglomerates of these smaller nuclei. The transitional particles were an intermediate zone between the slow growth rhombohedral/cubical particles and the agglomerated small nuclei spherical particles. We speculate the substantial roughness at the surface is due to the agglomeration of partially formed slower-growing particles. Also of note was that an increase in NH_4HCO_3:$MnSO_4$ ratio decreases inoculation time and shifts the particle morphology transitions to lower Mn^{2+} concentrations. This is also consistent with the interplay between the number of nuclei formed as the solubility of $MnCO_3$ is dependent on both the Mn^{2+} concentration and the CO_3^{2-} concentration, thus increasing the relative NH_4HCO_3:$MnSO_4$ ratio increases the nucleation rate by driving precipitation forward more quickly.

It is important to understand the morphologies we have reported in the context of typical carbonate battery precursors reported in the literature. First, all of our synthesis was at relatively low concentrations specifically such that we could assess the interplay between solution chemistry and morphology by accessing these different nucleation and growth regimes. While our synthesis does not exceed 12 mM Mn^{2+} concentration, 2 M concentrations of Mn^{2+} and other transition metal ions are not uncommon for carbonate battery precursors in the literature[16]. Our low concentrations allow us to access the diversity of morphologies reported, and also enable us to generate particle populations with relatively low polydispersity. Another important consideration in precursor synthesis that we were not explicitly investigating in this study was stir rate. Multiple coprecipitation battery precursor studies in the literature have investigated stir rate effects on morphology and/or final material performance.[15,30] We will comment here that

changing stir rate also influenced our particle morphologies. An increase in impeller rpm from 500 to 4800 rpm resulted in particles that, though clefted, were spherical in overall morphology at synthesis conditions that would give cubical morphology particles at 500 rpm as shown in Figure 7. The detailed origins of the mixing-induced morphology transitions are not yet completely understood and will be an area of future investigations.

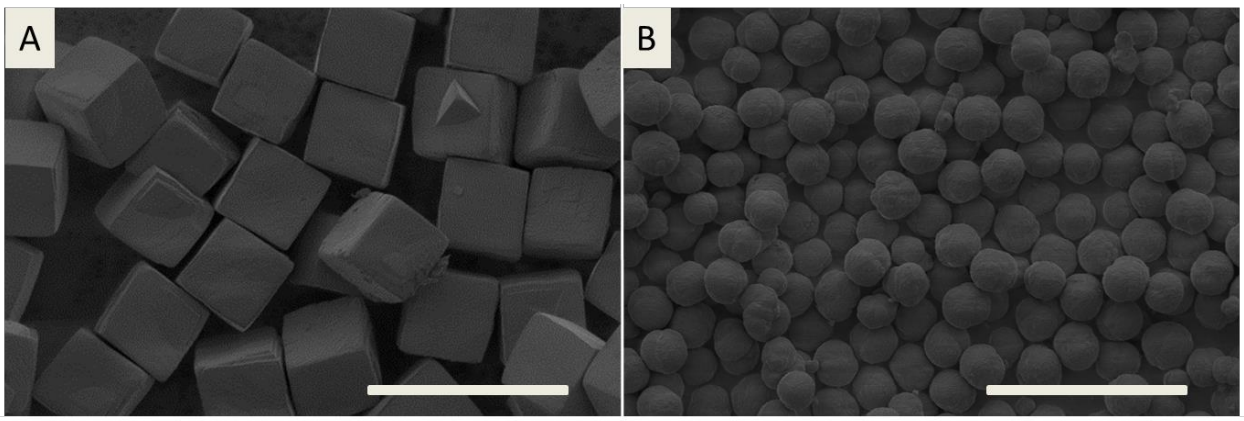

Figure 7. SEM images of particles prepared at 3 mM $MnSO_4$ and 40:1 NH_4HCO_3:$MnSO_4$ ratio with a stirring speed of (A) 500 rpm and (B) 4800 rpm. Scale bars correspond to 20 μm.

4.3 Solution Equilibria of the $MnCO_3$ System

The presence of an ammonium/ammonia source has previously been reported as being critical in morphology control of transition metal carbonate and hydroxide particles.[16,26] We similarly found the presence of an ammonia source to be crucial. Replacement of our typical NH_4HCO_3 coprecipitation reagent with $NaHCO_3$ resulted in dramatically reduced inoculation times and rapid formation of polydisperse particles as shown in Figure 8.

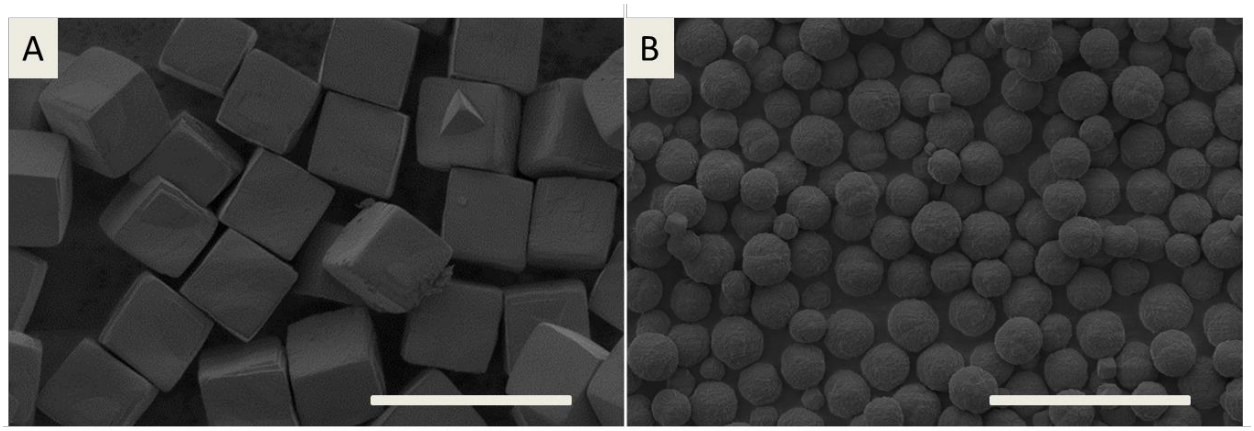

Figure 8. SEM image of particles prepared at 3 mM $MnSO_4$ and (A) 40:1 NH_4HCO_3:$MnSO_4$ ratio and (B) 40:1 $NaHCO_3$:$MnSO_4$ ratio. Scale bars correspond to 20 μm.

Ammonia has been shown to play a role in the coprecipitation of a variety of transition metals due to its ability to form aqueous soluble complexes with the transition metals.[26] These complexes have previously been reported to play a major role in the synthesis of transition metal hydroxide particles, in particular by enabling dissolution/recrystallization of the precipitates which facilitated ripening of particles into larger secondary particles[26]. To understand whether ammonia complexation was facilitating dissolution/recrystallization in our system, we performed calculations of the equilibrium concentrations of the solution species found in our system using the Medusa solution chemistry diagrams software. The equilibrium constants and major reactions associated with our synthesis are listed in Table 1.

Table 1. List of chemical reactions in the $MnCO_3$ Coprecipitation System and corresponding equilibrium constants.

Equilibrium Reaction	Log K
$Mn^{+2} + NH_3 \rightleftharpoons [Mn(NH_3)]^2$	1
$Mn^{+2} + 2NH_3 \rightleftharpoons [Mn(NH_3)_2]^2$	1.54
$Mn^{+2} + 3NH_3 \rightleftharpoons [Mn(NH_3)_3]^2$	1.70
$Mn^{+2} + 4NH_3 \rightleftharpoons [Mn(NH_3)_4]^2$	1.3
$NH_3 + H_2O \rightleftharpoons NH_4^+ + OH^-$	-4.8
$MnCO_3 \rightleftharpoons Mn^{2+} + CO_3^{-2}$	-10.6
$Mn(OH)_2 \rightleftharpoons Mn^{2+} + 2OH^-$	-12.7
$H_2O \rightleftharpoons H^+ + OH^-$	-14
$H_2CO_3 \rightleftharpoons HCO_3^- + H^+$	-6.4
$HCO_3^- \rightleftharpoons CO_3^{-2} + H^+$	-10.3
$Mn^{+2} + HCO_3^- \rightleftharpoons MnHCO_3^+$	1.27

Figure 9 shows the calculated equilibrium concentration of aqueous manganese species for all coprecipitation conditions tested. The dissolved manganese species are presented both in terms of total Mn solution concentration (Figure 9A) and as a fraction of the Mn that was available in the reaction vessel (Figure 9B). Total aqueous Mn species included were Mn^{+2}, $MnHCO_3^+$, $Mn(NH_3)^{+2}$, $Mn(NH_3)_2^{+2}$, and $MnOH^+$. The neutral pH (~7.5 for all synthesis conditions) normally results in minimal NH_3, with NH_4^+ being the dominant ammonia species in solution. Thus, the calculated $Mn(NH_3)^{+2}$ concentration was low for all conditions synthesized. Regardless of conditions used, at equilibrium our calculations predicted that soluble manganese species make up no more than 0.1% of total manganese in solution. Therefore, we conclude that ripening through aqueous dissolution and recrystallization of $MnCO_3$ in our system was unlikely. The results of Figure 9 are also presented in table form in the appendix.

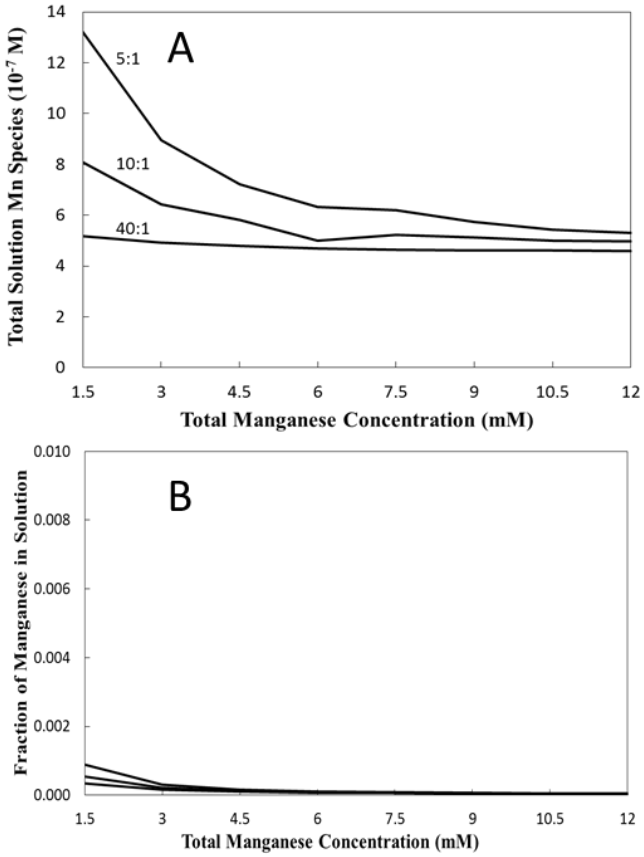

Figure 9. (A) Total calculated fraction of manganese that remains soluble at equilibrium as a function of total initial $MnSO_4$ concentration. Relative NH_4HCO_3:$MnSO_4$ ratios used in the calculations were 5:1 (top curve), 10:1 (middle curve), 40:1 (bottom curve) (B) Calculated fraction of all manganese available in solution which was soluble at equilibrium as a function of total initial $MnSO_4$ concentration. Relative NH_4HCO_3:$MnSO_4$ ratios used in the calculations were 5:1 (top curve), 10:1 (middle curve), 40:1 (bottom curve).

Further evidence that long-term dissolution and recrystallization does not play a major role in particle morphology for our system was provided through particle ripening experiments. We performed two coprecipitations using experimental conditions that gave us cubical and spherical particle morphologies, respectively (Figure 4B and Figure A1D). In these experiments, however, the particles were allowed to age for 7 hours instead of

being collected after 0.5 hours. SEMs from the long-time coprecipitations are shown in Figure 10.

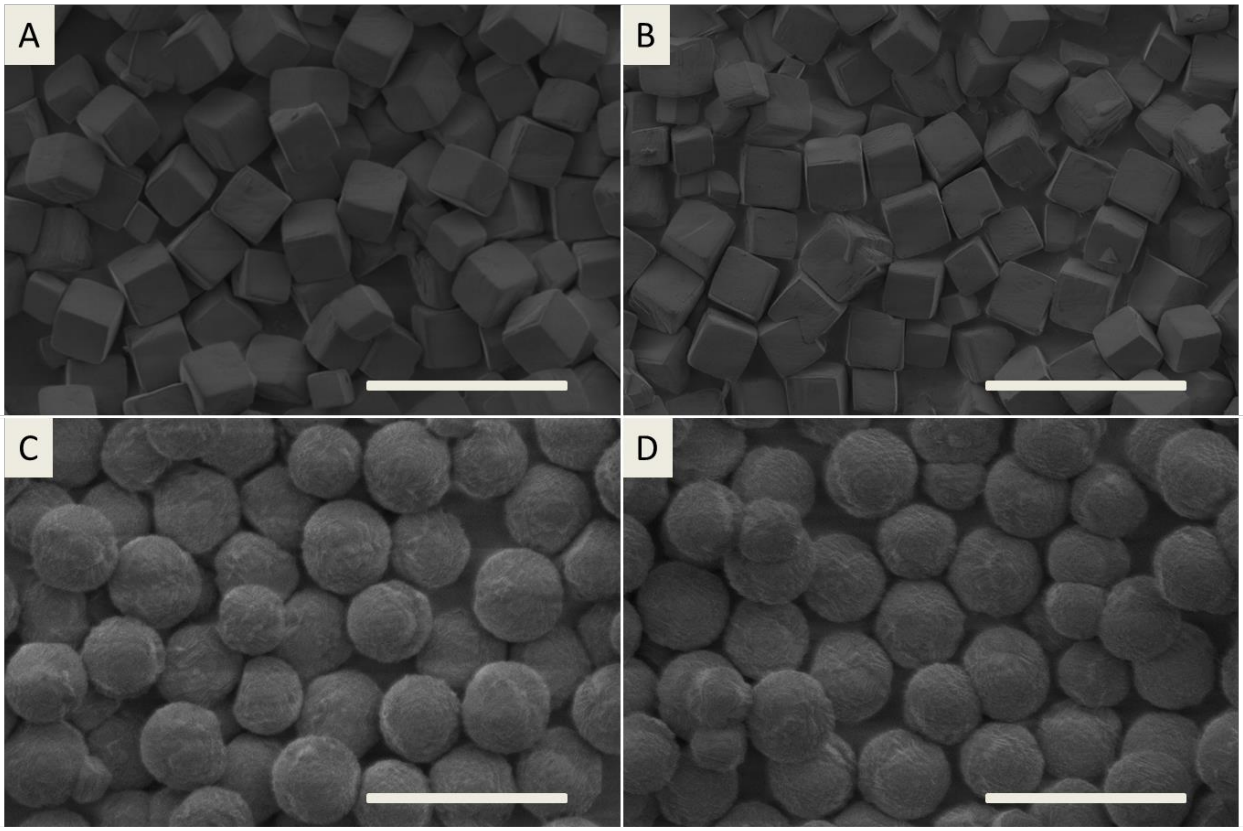

Figure 10. SEM image of cubical particles prepared with 3 mM $MnSO_4$ and a 40:1 NH_4HCO_3:$MnSO_4$ ratio and collected after (A) 30 minutes and (B) 7 hours. Spherical particles were prepared with 7.5 mM $MnSO_4$ and 10:1 NH_4HCO_3:$MnSO_4$ ratio and collected after (A) 30 minutes and (B) 7 hours. Scale bars correspond to 20 μm.

Over the 7 hour synthesis, the overall particle morphology does not change substantially relative to 0.5 hours. In the spherical particle case, only minor changes in surface roughness were observed, but there were no significant changes in overall particle size or shape. Cubical particles undergo no noticeable morphological changes.

While equilibrium calculations suggest ammonia-complex enabled dissolution/recrystallization does not facilitate long-term ripening and morphology changes, control experiments where ammonia was substituted with sodium (Figure 8) suggest that ammonia does play a role controlling particle morphology. One possibility was that even though the ammonia provides a relatively small amount of complexation of the manganese in solution, it was sufficient to lower supersaturation of the $MnCO_3$ enough to influence the nucleation and growth of $MnCO_3$ precipitates during the crucial early stages of the coprecipitation synthesis. We have qualitatively observed that the overall particle morphologies were frequently completed within the first few minutes of mixing of the reagent solutions. Detailed studies of the formation rates of $MnCO_3$ during the early stages of the coprecipitation will be necessary to ascertain the role that ammonia was playing at early synthesis stages to facilitate $MnCO_3$ final morphology.

4.4 Conversion of $MnCO_3$ to $LiMn_2O_4$

The detailed $MnCO_3$ synthesis studies described above were undertaken in an effort to achieve control over a diversity of morphologies and sizes of lithium-ion battery precursor particles. For these precursors to be useful in providing lithium-ion battery final active materials of tunable morphology, they must be able to retain their morphology after calcination and lithiation to convert the precursors to lithium-ion battery final active material.[3,7] To demonstrate that a variety of morphologies of active materials could be obtained via this route we chose two different $MnCO_3$ precursor morphologies, spherical and cubical, for conversion to $LiMn_2O_4$. As is shown in Figure 11 and Figure 12, the spherical $MnCO_3$ (Figure 11A) was successfully converted to spherical $LiMn_2O_4$ (Figure

11B) while retaining its overall spherical morphology and without sintering together into larger aggregates. Similarly, the cubical $MnCO_3$ (Figure 11C) was converted to cubical $LiMn_2O_4$ without significant fusing of particles into larger aggregates and while retaining the overall cubical morphology.

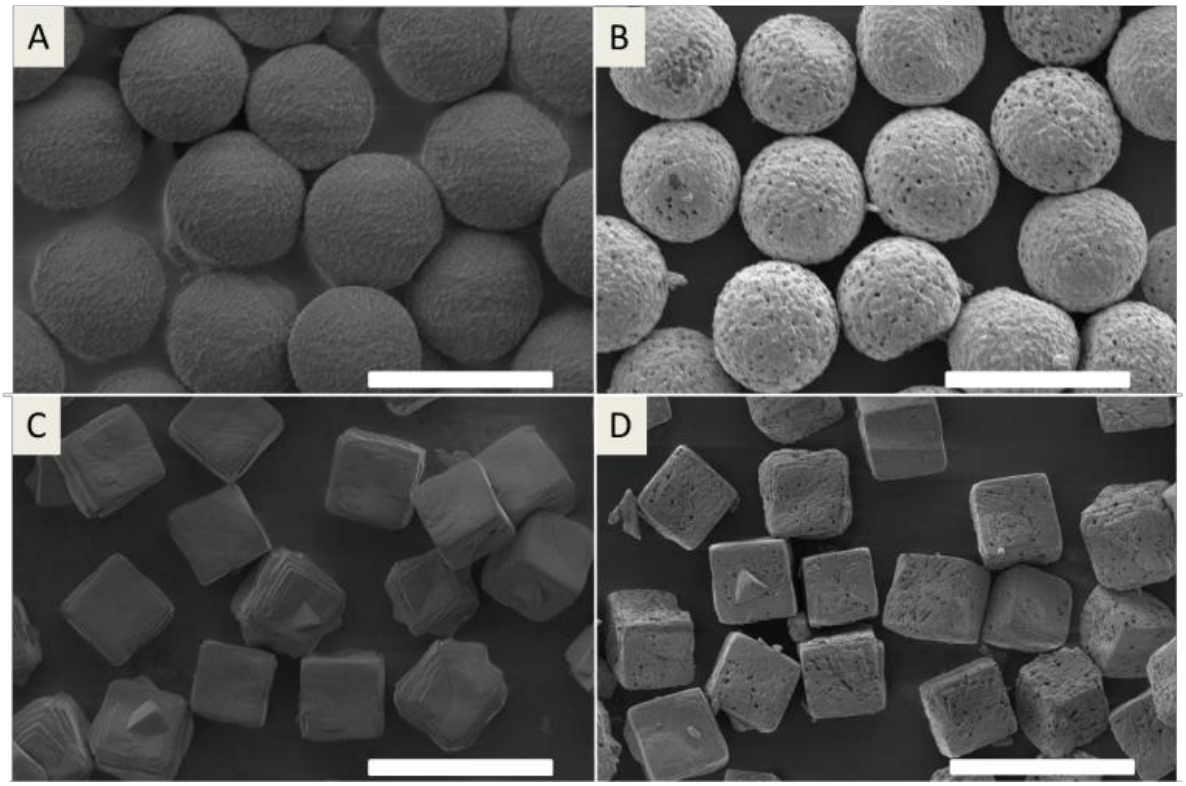

Figure 11. SEM images of (A) spherical $MnCO_3$ precursor particles and (B) the same particles after calcination to spherical $LiMn_2O_4$; and (C) cubical $MnCO_3$ precursor particles and (D) the same particles after calcination to cubical $LiMn_2O_4$. Scale bars correspond to 20 μm.

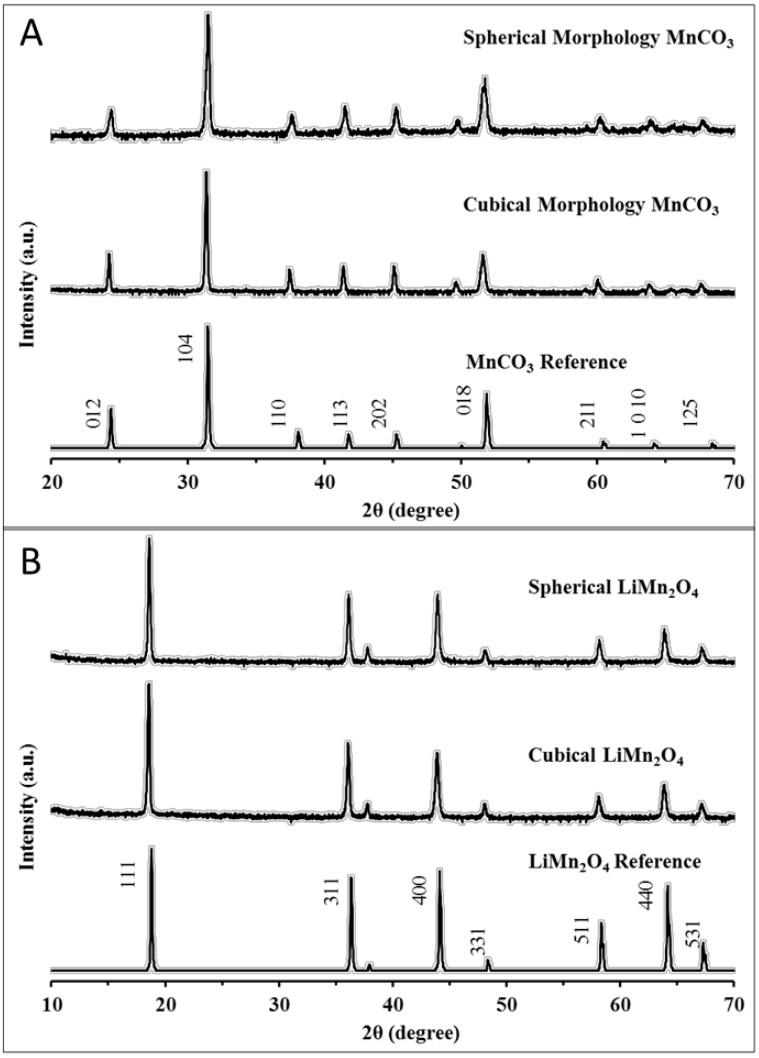

Figure 12. XRD patterns of the synthesized (A) $MnCO_3$ (reference[31]) and (B) $LiMn_2O_4$ (reference[32]) particles. The XRD patterns are from powders comprised of the particles found in Figure 11.

4.5 Electrochemical Testing of Obtained $LiMn_2O_4$

As a final confirmation of our $MnCO_3$ carbonate precursors as templates for tunable morphology lithium-ion battery cathode materials, we fabricated coin cells with cathodes comprised of the spherical and cubical $LiMn_2O_4$ particles shown in Figures 11B and 11D. The Li/$LiMn_2O_4$ half cells were cycled at increasing rates of ~C/20, C/10, C/2, and 1C (the 1C rate used for cycling was determined from using 148.2 mA/g of active $LiMn_2O_4$ material, the same rate was used on charge and discharge) between 3.4 V (vs. Li) to 4.2 V (vs. Li). Figure 13 shows the second charge/discharge cycle at C/20 for cathodes comprised of the spherical and cubical particles. The discharge capacities at the various rates can be found in the Supplemental Material, Figure 14. The charge/discharge characteristics of both the spherical and cubical $LiMn_2O_4$ active materials were consistent with those previously reported in the literature,[19] with two voltage plateaus at roughly 4.0 V and 4.1 V. Both coulombic and round trip energy efficiency for the cells was very high (>98% coulombic efficiency and >97% round trip energy efficiency at C/20), and the initial capacity >115 mAh/g for both materials. The spherical particles had slightly better rate capability and the cubical particles had slightly higher initial and low rate gravimetric capacity as seen in Figure 14, however, it would be premature to assign these observations at this point directly to the influences of particle morphology.

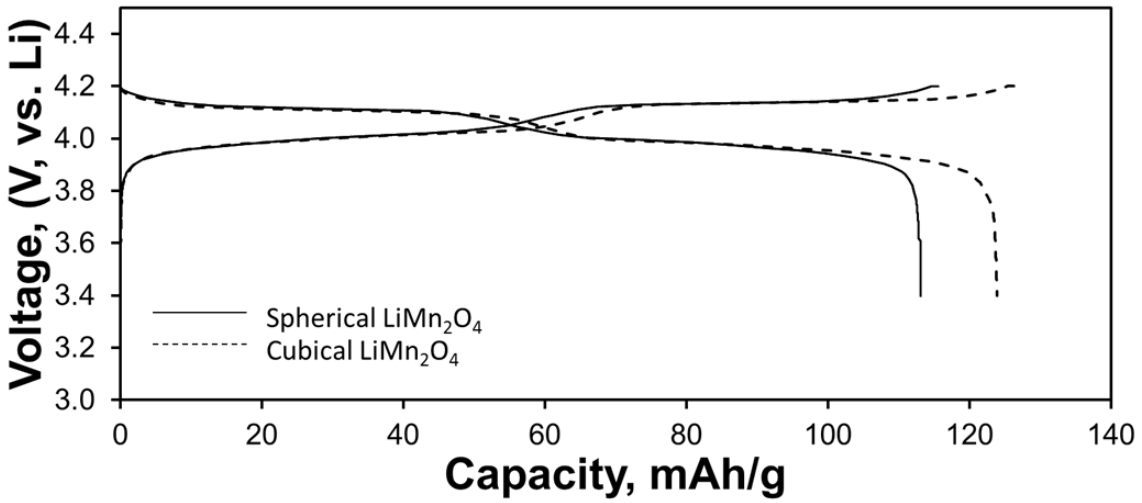

Figure 13. Charge/discharge curves from the second cycle of Li/$LiMn_2O_4$ half cells with cathodes containing $LiMn_2O_4$ active material particles with morphologies which are predominantly spherical and cubical. The rate of charge/discharge for both cells was approximately C/20.

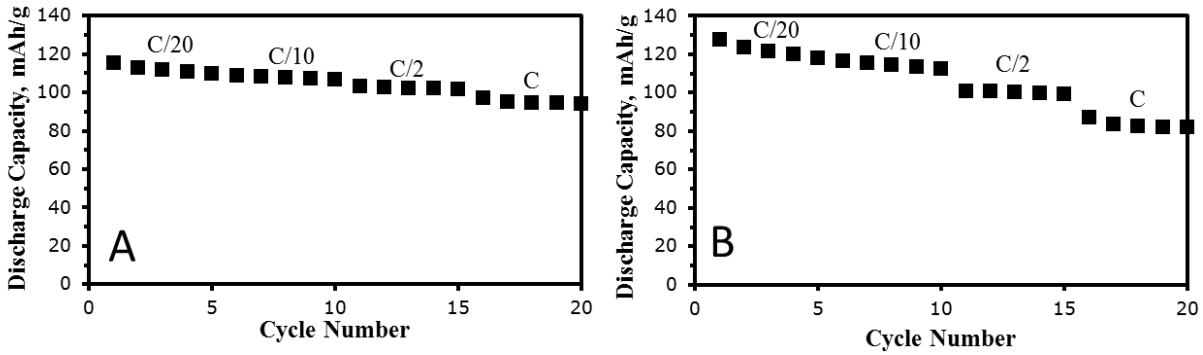

Figure 14. Discharge capacity of Li/$LiMn_2O_4$ half cells at increasing rates of charge/discharge (C/20, C/10, C/2, C). The cathode active material was composed of (A) spherical and (B) cubical morphology particles. Electrode particles used are those depicted in Figure 4. The rate used was the same for charge and discharge.

5. Conclusions

The influence of solution chemistry on resulting particle morphology during the synthesis of $MnCO_3$ precipitates was investigated in detail. It was found that moderate changes in reagent concentration could be used to tune the morphology and size of $MnCO_3$ particles, with shapes including rhombohedral, cubical, spherical, and cubical/spherical transitional and sizes ranging from 1 to 15 μm. These particles were very monodisperse relative to other common battery precursor particles reported in the literature. The resulting $MnCO_3$ morphologies were correlated with inoculation times and nucleation and growth of initial precipitates and appear to not be influenced by long-period dissolution/recrystallization processes, in contrast to processes that facilitate other precipitate systems in the literature. The controlled-morphology $MnCO_3$ precursors tuned via solution chemistry were used as templates to produce $LiMn_2O_4$, a lithium-ion battery cathode material. Synthesized $LiMn_2O_4$ particles retained the morphology of the $MnCO_3$ precursors, demonstrating that the described solution synthesis can be used to produce a diversity of controllable sizes and morphologies of lithium-ion battery active materials.

6. Recommendations

In order to further probe the growth mechanism of these $MnCO_3$ microparticles, it will be helpful to use in-situ techniques to study particle nucleation and growth dynamics. Collecting samples at early time points is difficult due to a variety of reasons including the necessity of rinsing the particles to remove excess salt, obtaining sufficient material quickly from the reactor, finding a particle sizing method which is reliable for both transitionary nanoparticles and 10 μm product particles, and overall speed of the process making it difficult to manipulate samples in a reliable manner. Although it's difficult to directly analyse the particles, the growth rate may be measurable through the use of ion probes or UV-Vis Spectroscopy. This would allow for insight into the initial nucleation and growth kinetics of the process which have been shown to be the main determinant of particle morphology for the conditions described in this manuscript.

This library of monodisperse $LiMn_2O_4$ particles serves as an excellent starting point for future studies on the relationship of particle morphology to electrode architectures. Recent publications have shown the potential of using X-ray tomography to create high resolution 3D models of actual battery electrodes.[14,33] Utilizing X-ray tomography will allow for more complete characterization and understanding of the hierarchical transport mechanisms in Li-ion batteries. In particular it provides a way to reliably measure electrode-level structures such as pore morphology and tortuosity.

The cubical $LiMn_2O_4$ particles may provide some interesting opportunities for the synthesis of 2D particle electrodes. These particle electrodes could potentially eliminate

additives and have a monolayer thickness. $LiMn_2O_4$ particles are easily suspended at an air-water interface, and can be densified and transferred to a current collector using a Langmuir-Blodgett trough. The faceted structure of the cubical particles could enhance adherence and electrical contact with the electrode after transfer, and allow for studies that isolate the individual particle's transport resistances.

References

1. Thackeray, M. M., Wolverton, C. & Isaacs, E. D. Electrical energy storage for transportation—approaching the limits of, and going beyond, lithium-ion batteries. *Energy Environ*. *Sci*. **5,** 7854 (2012).

2. Goodenough, J. B. & Kim, Y. Challenges for Rechargeable Li Batteries †. *Chem*. *Mater*. **22,** 587–603 (2010).

3. Koenig, G. M., Belharouak, I., Deng, H., Sun, Y. & Amine, K. Composition-Tailored Synthesis of Gradient Transition Metal Precursor Particles for Lithium-Ion Battery Cathode Materials. *Chem*. *Mater*. **23,** 1954–1963 (2011).

4. Belharouak, I., Koenig, G. M. & Amine, K. Electrochemistry and safety of Li4Ti5O12 and graphite anodes paired with LiMn2O4 for hybrid electric vehicle Li-ion battery applications. *J*. *Power Sources* **196,** 10344–10350 (2011).

5. Kim, D. K. *et al*. Spinel LiMn 2 O 4 Nanorods as Lithium Ion Battery Cathodes. *Nano Lett*. **8,** 3948–3952 (2008).

6. Lin, H. B. *et al*. Porous LiMn2O4 cubes architectured with single-crystalline nanoparticles and exhibiting excellent cyclic stability and rate capability as the cathode of a lithium ion battery. *J*. *Mater*. *Chem*. *A* **2,** 9272 (2014).

7. Wang, D., Belharouak, I., Koenig, G. M., Zhou, G. & Amine, K. Growth mechanism of Ni0.3Mn0.7CO3 precursor for high capacity Li-ion battery cathodes. *J*. *Mater*. *Chem*. **21,** 9290 (2011).

8. Wang, B., Wu, X.-L., Shu, C.-Y., Guo, Y.-G. & Wang, C.-R. Synthesis of CuO/graphene nanocomposite as a high-performance anode material for lithium-ion batteries. *J*. *Mater*. *Chem*. **20,** 10661 (2010).

9. Mei, R., Song, X., Yang, Y., An, Z. & Zhang, J. Plate-like LiFePO4 crystallite with preferential growth of (010) lattice plane for high performance Li-ion batteries. *RSC Adv*. **4,** 5746 (2014).

10. Li, Z., Xu, J., Chen, X., Zhou, Q. & Shang, T. A simple hydrothermal route to synthesis of rod-like MnOOH and spindle-shaped MnCO3. *Colloid Polym*. *Sci*. **289,** 1643–1651 (2011).

11. Ryu, W.-H., Lim, S.-J., Kim, W.-K. & Kwon, H. 3-D dumbbell-like LiNi1/3Mn1/3Co1/3O2 cathode materials assembled with nano-building blocks for lithium-ion batteries. *J*. *Power Sources* **257,** 186–191 (2014).

12. Hong, S.-K., Mho, S.-I., Yeo, I.-H., Kang, Y. & Kim, D.-W. Structural and electrochemical characteristics of morphology-controlled Li[Ni0.5Mn1.5]O4 cathodes. *Electrochim*. *Acta* **156,** 29–37 (2015).

13. Koenig, G. M., Belharouak, I., Wu, H. M. & Amine, K. Hollow lithiated metal oxide particles as lithium-ion battery cathode materials. *Electrochim*. *Acta* **56,** 1426–1431 (2011).

14. Ebner, M., Chung, D.-W., García, R. E. & Wood, V. Tortuosity Anisotropy in Lithium-Ion Battery Electrodes. *Adv*. *Energy Mater*. **4,** n/a–n/a (2014).

15. Lee, M.-H., Kang, Y.-J., Myung, S.-T. & Sun, Y.-K. Synthetic optimization of Li[Ni1/3Co1/3Mn1/3]O2 via co-precipitation. *Electrochim*. *Acta* **50,** 939–948 (2004).

16. Park, S.-H., Kang, S.-H., Belharouak, I., Sun, Y. K. & Amine, K. Physical and electrochemical properties of spherical Li1+x(Ni1/3Co1/3Mn1/3)1−xO2 cathode materials. *J*. *Power Sources* **177,** 177–183 (2008).

17. Tarascon, J. M. *et al*. Synthesis Conditions and Oxygen Stoichiometry Effects on Li Insertion into the Spinel LiMn O. *J*. *Electrochem*. *Soc*. **141,** 1421–1431 (1994).

18. Ferg, E. & Gummow, R. Spinel Anodes for Lithium-Ion Batteries. *J*. *Electrochem*. *Soc*. **141,** 9–12 (1994).

19. Tarascon, J. & Wang, E. The Spinel Phase of LiMn2 O 4 as a Cathode in Secondary Lithium Cells. *J*. *Electrochem*. *Soc*. **138,** 1–6 (1991).

20. Duan, X., Ma, J., Lian, J., Kim, T. & Zheng, W. A novel surfactant-free route to MnCO3 steep rhombohedra crystals and their large-scale assembly into regular elongated patterns in a mixed solvent. *Chem*. *Commun*. *(Camb)*. **46,** 7133–5 (2010).

21. Hamada, S., Kudo, Y., Okada, J. & Kano, H. Preparation of Monodispersed Manganese (IV) Oxide Particles from Manganese (11) Carbonate Formation of Monodispersed Spherical Manganese (II) Carbonate Particles Preparation of Monoclinic-Like Manganese To determine the zeta potential and surface. *J*. *Colloid Interface Sci*. **118,** 356–365 (1987).

22. Zhu, H., Stein, E. W., Lu, Z., Lvov, Y. M. & McShane, M. J. Synthesis of Size-Controlled Monodisperse Manganese Carbonate Microparticles as Templates for Uniform Polyelectrolyte Microcapsule Formation. *Chem*. *Mater*. **17,** 2323–2328 (2005).

23. Lee, H.-K., Sakemi, D., Selyanchyn, R., Lee, C.-G. & Lee, S.-W. Titania nanocoating on MnCO3 microspheres via liquid-phase deposition for fabrication of template-assisted core-shell- and hollow-structured composites. *ACS Appl*. *Mater*. *Interfaces* **6,** 57–64 (2014).

24. Wan, C., Cheng, M. & Wu, D. Synthesis of spherical spinel LiMn2O4 with commercial manganese carbonate. *Powder Technol*. **210,** 47–51 (2011).

25. Zhu, Z., Zhang, D. & Yu, H. Preparation of spherical hierarchical LiNi0.5Mn1.5O4 with high electrochemical performances by a novel composite co-precipitation method for 5V lithium ion secondary batteries. *Electrochim*. *Acta* **115,** 290–296 (2014).

26. Bommel, A. Van & Dahn, J. of the Growth Mechanism of Coprecipitated Spherical and Dense Nickel, Manganese, and Cobalt-Containing Hydroxides in the Presence of Aqueous Ammonia. *Chem*. *Mater*. **21,** 1500–1503 (2009).

27. Li, J. *et al*. Unravelling the Impact of Reaction Paths on Mechanical Degradation of Intercalation Cathodes for Lithium-Ion Batteries. *J*. *Am*. *Chem*. *Soc*. 1–4 (2015). doi:10.1021/jacs.5b06178

28. Schneider, C. a, Rasband, W. S. & Eliceiri, K. W. NIH Image to ImageJ: 25 years of image analysis. *Nat*. *Methods* **9,** 671–675 (2012).

29. Wayland, R. G. Composition, Specific Gravity, and Refractive Indices of Rhodochrosite; Rhodochrosite from Butte, Montana. *Am*. *Mineral*. **27,** 614–628 (1942).

30. Camardese, J., Abarbanel, D. W., McCalla, E. & Dahn, J. R. Synthesis of Spherical Core-Shell Ni(OH)2-Ni1/2Mn1/2(OH)2 Particles via a Continuously Stirred Tank Reactor. *J*. *Electrochem*. *Soc*. **161,** A890–A895 (2014).

31. Hanawalt, J. et al. *Anal*. *Chem*. **10,** 475 (1938).

32. Schmier. *Naturwissenschaften* **52,** 392 (1965).

33. Ebner, M., Geldmacher, F., Marone, F., Stampanoni, M. & Wood, V. X-Ray Tomography of Porous, Transition Metal Oxide Based Lithium Ion Battery Electrodes. *Adv*. *Energy Mater*. **3,** 845–850 (2013).

Appendix

Appendix: SEM Images of 1:1, 5:1, 10:1 NH_4HCO_3:$MnSO_4$ $MnCO_3$ Particles

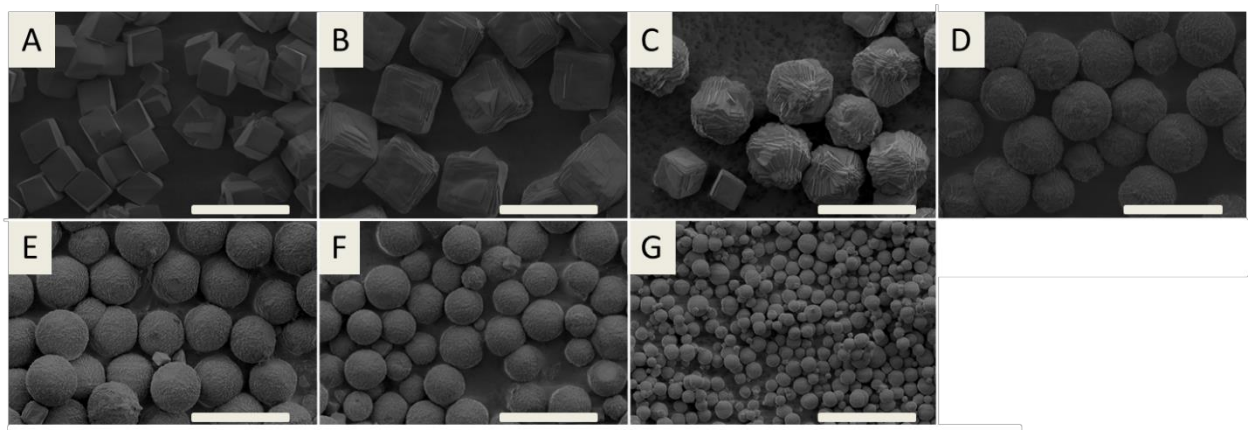

Figure A1. SEM images of $MnCO_3$ particles prepared with a 10:1 ratio of NH_4HCO_3 to $MnSO_4$ and ascending concentration of $MnSO_4$: (A) 3 mM $MnSO_4$, (B) 4.5 mM $MnSO_4$, (C) 6 mM $MnSO_4$, (D) 7.5 mM $MnSO_4$, (E) 9 mM $MnSO_4$, (F) 10.5 mM $MnSO_4$, (G) 12 mM $MnSO_4$. A synthesis was performed at 1.5 mM $MnSO_4$; however, there were no recoverable particles. Scale bars correspond to 20 μm.

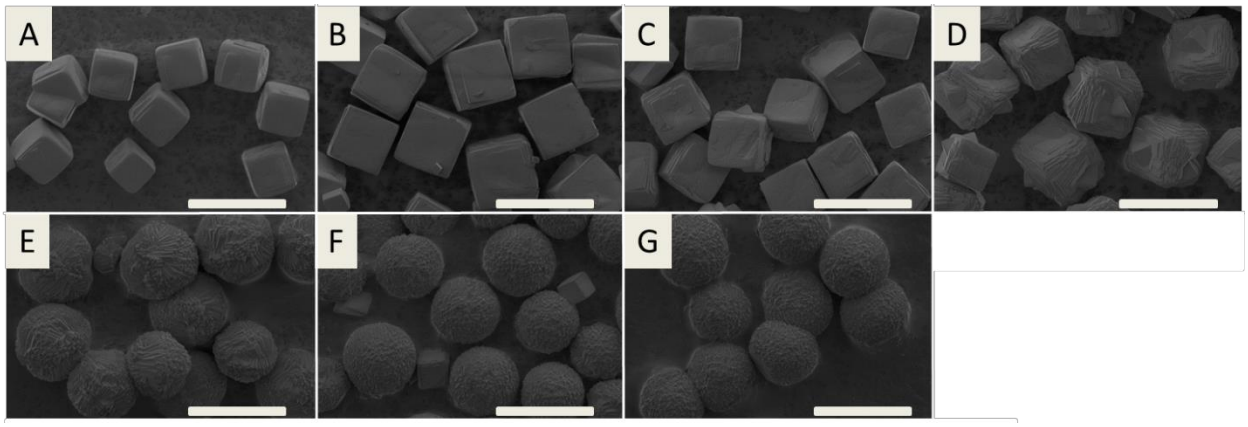

Figure A2. SEM images of $MnCO_3$ particles prepared with a 5:1 ratio of NH_4HCO_3 to $MnSO_4$ and ascending concentration of $MnSO_4$: (A) 3 mM $MnSO_4$, (B) 4.5 mM $MnSO_4$, (C) 6 mM $MnSO_4$, (D) 7.5 mM $MnSO_4$, (E) 9 mM $MnSO_4$, (F) 10.5 mM $MnSO_4$, (G) 12 mM $MnSO_4$. A synthesis was performed at 1.5 mM $MnSO_4$; however, there were no recoverable particles. Scale bars correspond to 20 μm.

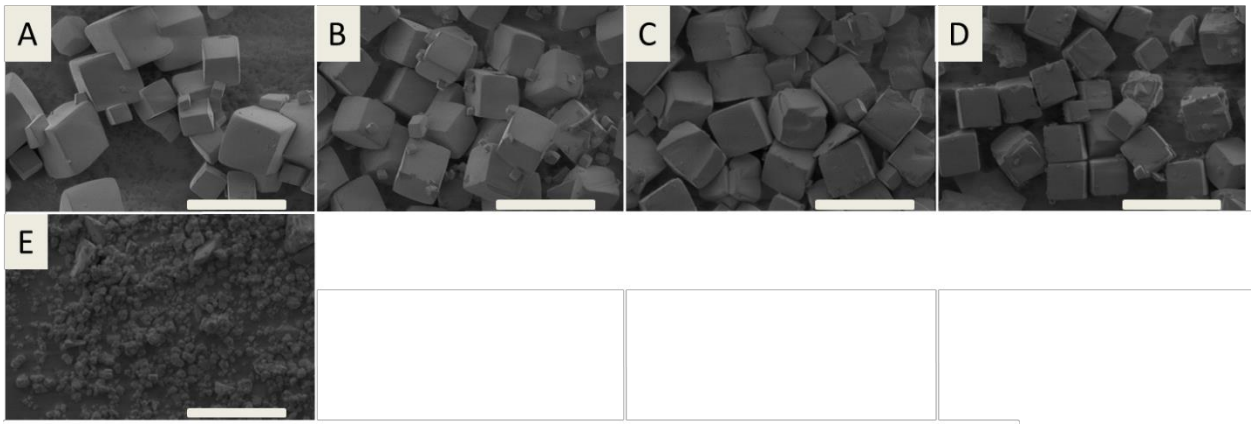

Figure A3. SEM images of $MnCO_3$ particles prepared with a 1:1 ratio of NH_4HCO_3 to $MnSO_4$ and ascending concentration of $MnSO_4$: (A) 6 mM $MnSO_4$, (B) 7.5 mM $MnSO_4$, (C) 9 mM $MnSO_4$, (D) 10.5 mM $MnSO_4$, (E) 12 mM $MnSO_4$. Synthesis was also performed at 1.5 mM $MnSO_4$, 3 mM $MnSO_4$, and 4.5 mM $MnSO_4$, however, there were no recoverable particles at these conditions. Scale bars correspond to 20 μm.

Appendix: Table Format of Medusa Calculation Output shown in Figure 3

Table A1. Manganese in Solution as a % of Total Manganese

	Initial $MnSO_4$ Concentration (mM)							
	1.5	3	4.5	6	7.5	9	10.5	12
40:1	0.034	0.016	0.011	0.008	0.006	0.005	0.004	0.004
10:1	0.054	0.021	0.013	0.008	0.007	0.006	0.005	0.004
5:1	0.088	0.030	0.016	0.011	0.008	0.006	0.005	0.004
1:1	4.143	3.672	1.178	0.863	0.660	0.525	0.440	0.344

Table A2. Total Concentration of Aqueous Manganese (10^{-5} M)

	Initial $MnSO_4$ Concentration (mM)							
	1.5	3	4.5	6	7.5	9	10.5	12
40:1	4143	3672	1178	863	660	525	440	344
10:1	88	30	16	11	8	6	5	4
5:1	54	21	13	8	7	6	5	4
1:1	34	16	11	8	6	5	4	4

Appendix: Cross-section and top-down images of composite electrodes.

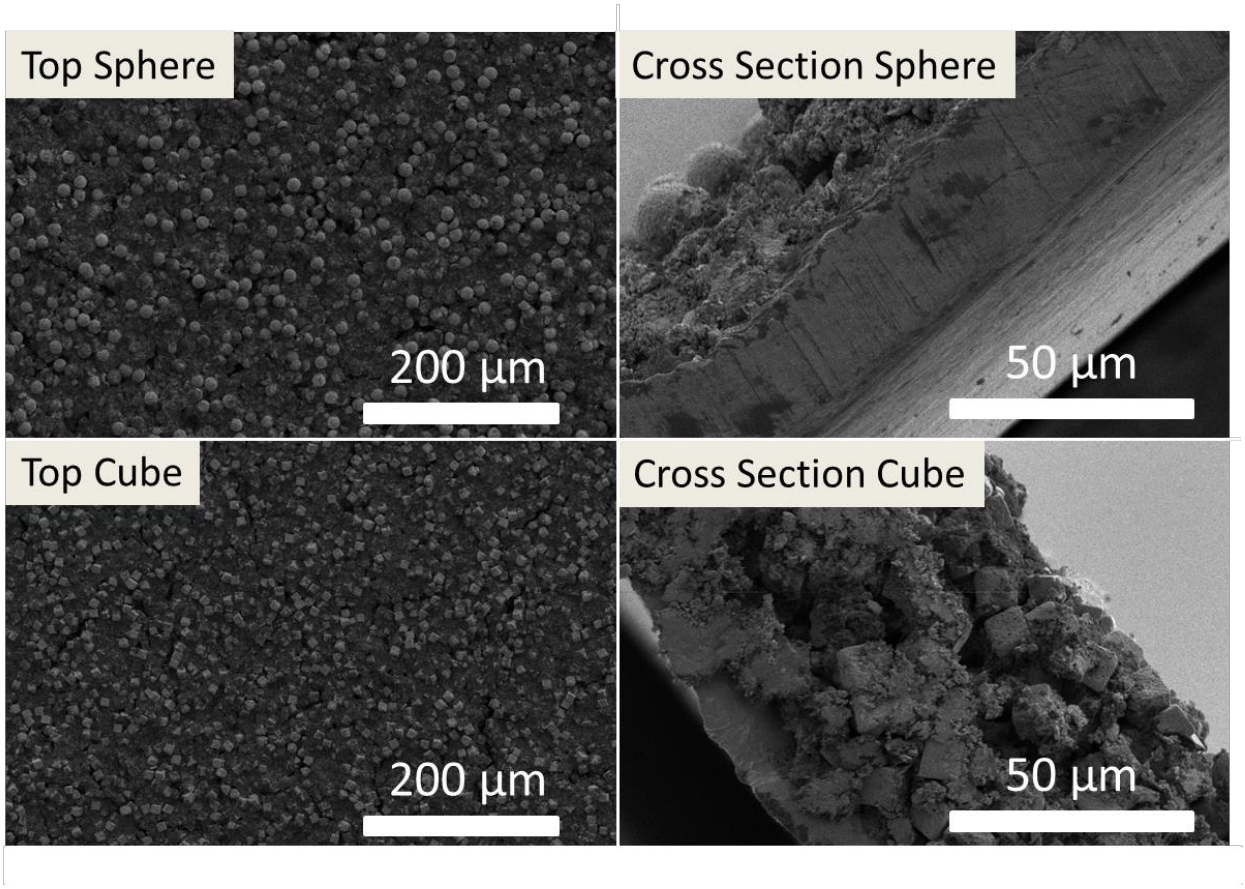

Figure A4. Composite Li-ion battery cathodes coated on an aluminium current collector. These electrodes were prepared with 80 wt% active material particles, 10 wt% carbon black, and 10% PVDF binder. This loading is typical for an academic battery, but low for commercial electrodes where less additives are typically used in order to increase the energy density of the electrode.